Eur. Phys. J. D **28**, 125–133 (2004)
DOI: 10.1140/epjd/e2003-00288-0

THE EUROPEAN PHYSICAL JOURNAL D

Time-of-flight resolved transmission-grating diffraction of molecular beams

W. Schöllkopf[a], R.E. Grisenti[b], and J.P. Toennies

Max-Planck-Institut für Strömungsforschung, Bunsenstraße 10, 37073 Göttingen, Germany

Received 13 July 2003 / Received in final form 3 September 2003
Published online 21 October 2003 –

Abstract. Diffraction of molecular beams of CH_3F, CHF_3, and metastable He^* and Ne^* from a 100-nm-period micro-fabricated transmission grating has been observed. Due to the finite velocity spread and the corresponding temporal coherence of the molecular beams, diffraction peaks of only the first few orders are resolved in total-intensity measurements, while higher order peaks are increasingly broadened and smeared-out. Combining time-of-flight (TOF) measurements with angular scans has allowed to observe TOF-resolved diffraction data which yield full resolution of all detected diffraction peaks. Here, this method has been applied to investigate atom/molecule-surface interactions. In general, it can be used to observe resolved diffraction patterns of a wide range of atomic and molecular beams whose broad velocity distributions prevent peak-resolution in conventional total-intensity measurements.

PACS. 39.20.+q Atom interferometry techniques – 03.75.Be Atom and neutron optics – 07.77.Gx Atomic and molecular beam sources and detectors – 34.50.Dy Interactions of atoms and molecules with surfaces; photon and electron emission; neutralization of ions

1 Introduction

The diffraction of atoms and molecules by micro-fabricated transmission gratings has recently been demonstrated for beams of a number of different atoms and molecules [1–11]. The systems studied include sodium atoms [1], metastable helium [2,11] and metastable neon [11] atoms, ground state rare gas atoms including helium [3,7], diatomic molecules of sodium (Na_2) [4] and deuterium (D_2) [3,7], helium clusters from He_2 up to He_{26} [3,5,6,9,10], small hydrogen clusters $(H_2)_N$ and deuterium clusters $(D_2)_N$ [3], as well as fullerene molecules [8]. Aside from their academic interest as further demonstrations of wave-particle dualism these experiments have recently been shown to provide new opportunities for measurements of molecular properties. Already in 1994, because of its non-destructive nature, grating diffraction provided the first unambiguous evidence for the existence of the very weakly bound helium dimer [3,5]. Furthermore, from the analysis of the diffraction peak intensities up to the seventh order it has been possible to determine quantitatively the attractive long range particle-surface van der Waals potentials between several ground state [7] and metastable rare gas atoms [11], as well as H_2 and D_2 molecules [7] with the surfaces of the silicon nitride grating bars. Recently, a similar analysis has made it possible to determine the geometrical size and, from this, the binding energy of the helium dimer [9]. Another interesting application is the investigation of the kinetics governing the growth of small helium clusters allowing for the study of homogeneous nucleation as the mechanism of condensation in a purified gas [10]. In addition, analysis of the intensities of atomic helium beams diffracted from a 100-nm-period silicon nitride grating has been used to characterize in detail shape, dimensions, and uniformity of the nanoscale grating bars [12].

In most of these diffraction experiments the angular resolution of the diffraction peaks has not been limited by the finite lateral extension (width) of the diffraction grating but rather by the spatial and temporal coherence of the incident molecular beam. The spatial coherence of the incident molecular beam is given by its angular width $\Delta\vartheta^{(0)}$ (full width at half maximum (FWHM)) which is determined by the two collimating slits between beam source and diffraction grating. The temporal coherence is limited by the longitudinal velocity spread Δv (FWHM) of the incident beam with a most probable velocity denoted by u.

[a] *Present address:* Fritz-Haber-Institut der Max-Planck-Gesellschaft, Abteilung Molekülphysik, Faradayweg 4-6, 14195 Berlin, Germany.
e-mail: wschoell@fhi-berlin.mpg.de

[b] *Present address:* Johann Wolfgang Goethe-Universität, Institut für Kernphysik, August-Euler-Str. 6, 60486 Frankfurt, Germany.

Thus, the overall angular width (FWHM) of the nth-order diffraction peak is given by[1]

$$\Delta\vartheta^{(n)} = \sqrt{\left(\Delta\vartheta^{(0)}\right)^2 + \left(\vartheta^{(n)}\frac{\Delta v}{u}\right)^2}, \qquad (1)$$

where $\vartheta^{(n)}$ denotes the nth-order diffraction angle. Even for highly expanded helium atom beams, which are characterized by exceedingly narrow velocity distributions with $\Delta v/u \simeq 1\%$, an increase in peak broadening with increasing diffraction order ($0 \leq n \leq 9$) has been observed and analyzed to be due to the second term in equation (1) [12].

This limitation in the resolution is especially severe for molecular beams which inherently have rather broad Maxwellian-like velocity distributions. For polyatomic molecules jet expansions with large source pressures are not possible because of the tendency to form large clusters. Using seeded beams to decrease the velocity spread has the disadvantage that the corresponding increase in beam velocity leads to a reduced de Broglie wavelength. Thus, for many molecules and atoms the limited temporal coherence may prevent the observation of highly resolved diffraction spectra. For C_{70} fullerene molecules this limitation was recently circumvented by selecting a narrow range out of the parabolic trajectories of the heavy molecules in the gravitational field [13] or by employing a mechanical velocity selector [14]. In these techniques, however, molecules outside a narrow interval within the broad velocity distribution are discarded leading to a corresponding loss of signal and of information.

In the present article a new method, first described in a different context in references [15–17], is used to overcome this limitation and is demonstrated by the diffraction of molecular beams of CH_3F molecules, metastable helium atoms (He^*), and metastable neon atoms (Ne^*) by a 100-nm-period transmission grating. Instead of measuring the total intensity at each angle, in the new technique the time-of-flight distribution is measured at each deflection angle. From the data the angular distribution for a given time-of-flight is extracted leading to a better resolved diffraction pattern by effectively eliminating the second term on the right hand side of equation (1). This technique makes it possible to extend high resolution transmission grating diffraction to a wider range of particles.

Following a brief description of the apparatus and the experimental procedures in Section 2, the results on time-of-flight spectra and improving the resolution are presented in Section 3. The article closes with conclusions in Section 4.

[1] This equation has been derived in reference [12] (Eq. (32)) by approximating the incident beam angular and velocity distributions by Gaussians. For not too large velocity spreads, their convolution results in a Gaussian angular spread, the variance of which is given by the sum of both variances.

Table 1. Source pressure P_0, mean velocity u, relative width of the velocity distribution $\Delta v/u$, and mean de Broglie wavelengths λ of the atoms and molecules in the grating diffraction experiments.

species	P_0 [bar]	u [m/s]	$\Delta v/u$ [%]	λ [pm]
CH_3F	2.0	754	31	15.5
CHF_3	1.5	517	34	11
He^* ($^3S_1$)	2.0	2347	27	42.5
Ne^* (^3P_J)	1.6	873	45	22.6

2 Experimental

The experiments were carried out with two similar molecular-beam grating-diffraction apparatus. Apparatus A, described previously [12], was used in the CH_3F and CHF_3 experiments, while the metastable-atom experiments were carried out with Apparatus B ("MAGIE I"), described previously in reference [9].

In Apparatus A the molecular beam is produced by expansion of pure gas of CH_3F (99.0% purity) or CHF_3 (99.9%) through an orifice (5 ± 1 μm nominal diameter and about 2 μm long) into vacuum. The source is at room temperature ($T_0 \approx 300$ K) and the source pressures are limited to about $P_0 = 4$ bar by the onset of extensive condensation to clusters, which is apparent in the mass spectra as described below. The pressure in the vacuum chamber increases from 2.5×10^{-7} mbar, if no gas is applied to the source, to about 3×10^{-5} mbar at $P_0 = 4$ bar, but had no significant effect on the beam velocity distribution and intensity.

In Apparatus B the beam of metastable helium ($He\ ^3S_1$) or neon ($Ne\ ^3P_J$) atoms is produced by a continuous discharge in the free-jet expansion zone of a sapphire nozzle (0.16 mm orifice diameter) driven by a DC voltage of -1.1 kV (He^*) or -0.9 kV (Ne^*) between a tungsten wire inside the sapphire source and the skimmer (0.72 mm orifice diameter). At source pressures of $P_0 = 2.0$ bar (He^*) and 1.6 bar (Ne^*) the observed mean velocities of the metastable-atom beams, listed in Table 1, correspond to effective source temperatures of $T_0^{\rm eff}(He^*) = 530$ K and $T_0^{\rm eff}(Ne^*) = 370$ K.

In both apparatus the beam is collimated by two narrow slits located between the skimmer and the grating as shown in Figure 1. The dimensions and positions of skimmers, slits, and gratings for both apparatus are listed in Table 2. The transmission grating, located downstream from the second slit, can be rotated by Θ_0 around an axis which is parallel to the grating bars and perpendicular to the detection plane allowing for normal and off-normal incidence [12]. High angular resolution of the detector is achieved by a third, 25 μm-wide slit located downstream from the grating in front of the detector entrance. The given widths and positions of the slits result in overall effective angular resolutions $\vartheta^{(0)}$ of about 70 μrad FWHM (Apparatus A) and 100 μrad FWHM (Apparatus B) as determined from the measured angular intensity profile of

Table 2. Dimensions and the overall angular resolution of the two apparatus. The characteristic dimension is the nominal diameter for nozzle-orifice and skimmer; the nominal slit width for the collimating slits (5 mm high); the disk diameter for the chopper; the measured geometrical slit width s_0 for the 100-nm-period grating; and the estimated length for the ionizer. The position along the molecular beam axis is given with respect to the skimmer opening. The angular resolution is the width (FWHM) of the angular intensity profile (apparatus function) observed without a grating in the beam path.

device	Apparatus A		Apparatus B ("MAGIE I")	
	characteristic dimension	position [mm]	characteristic dimension	position [mm]
nozzle orifice	$\varnothing = 5\,\mu$m	≈ -10	$\varnothing = 160\,\mu$m	≈ -10
skimmer	$\varnothing = 0.39$ mm	0	$\varnothing = 0.72$ mm	0
slit 1	$10\,\mu$m	56	$20\,\mu$m	150
chopper	$\varnothing = 10$ cm	64	$\varnothing = 14$ cm	450
slit 2	$10\,\mu$m	475	$10\,\mu$m	1000
grating	$s_0 = 53.4$ nm	500	$s_0 = 66.8$ nm	1150
slit 3	$25\,\mu$m	1020	$25\,\mu$m	1530
ionizer/channeltron	$l_{\rm ioni} \simeq 5$ mm	1384	—	2400
angular resolution	70 μrad		100 μrad	

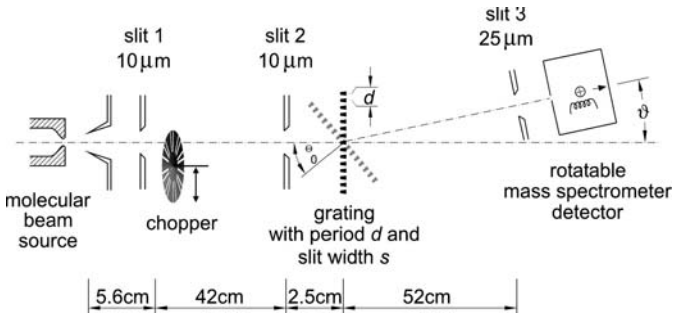

Fig. 1. Experimental setup of Apparatus A. The 100-nm-period transmission grating can be rotated by Θ_0 around an axis perpendicular to the detection plane. Slits, grating, and the chopper disc can be introduced into the beam path independently. The geometry parameters are listed in Table 2.

the beam without grating. Hence, for the given de Broglie wavelengths λ listed in Table 1, the collimation provides for an effective lateral coherence length $l_{\rm eff} = \lambda/\vartheta^{(0)}$ of about 0.22 μm (CH_3F), 0.16 μm (CHF_3), 0.43 μm (He*), and 0.23 μm (Ne*), indicating that, in each case, diffraction from a 100-nm-period grating is expected to be observable.

The transmission diffraction gratings are made out of non-stoichiometric silicon nitride (SiN_X) and have a period of $d = 100$ nm. They have been manufactured by Tim Savas and Henry I. Smith at MIT using achromatic interferometric lithography and reactive ion etching [18]. Their overall dimensions are 200 μm in width and 5 mm in height. Grating A, used for the CH_3F and CHF_3 diffraction, is characterized by a geometrical slit width of $s_0 = 53.4 \pm 0.6$ nm, determined from an analysis of high-resolution helium atom beam diffraction intensities [7], and by a thickness (depth) of the bars of $t = 90$ nm, derived from an analysis of atomic beam transmission measurements as a function of Θ_0 as described in reference [12]. For Grating B, used in the He* and Ne* experiments, the corresponding dimensions were found to be $s_0 = 66.8$ nm and $t = 53$ nm [11].

In Apparatus A the molecules are detected by a home-made electron bombardment ionizer at an electron energy of 120 eV, and the resulting ions are subsequently mass selected in a magnetic mass spectrometer with a mass-resolution $m/\Delta m \approx 40$. To minimize the background count rates the vacuum in the detector chamber is maintained at less than 1×10^{-11} mbar. In Apparatus B the metastable atoms, due to their large internal energy of 19.8 eV (He*) and 16.6 eV (Ne*), are efficiently detected by a channeltron electron multiplier with an estimated quantum efficiency of close to unity for both, He* and Ne*. With this detector the background count-rate is inherently vanishingly small.

For time-of-flight (TOF) measurements, in Apparatus A, a pseudo-random sequence chopper is introduced into the beam path at 71 mm from the source ($L = 1.32$ m long flight path to ionizer). The 100-mm-diameter disk with two identical random sequences along the perimeter, each consisting of 127 slit and bar segments, was rotated at 218 revolutions per second resulting in a gate-time (i.e., the duration during which atoms pass through a slit segment) of $\tau_{\rm gate} = 18\,\mu$s. The detector counts were accumulated in 127 successive time-resolved memory channels with a single-channel width of $\tau_{\rm ch} = 18\,\mu$s synchronized to $\tau_{\rm gate}$. The finite length of the ionizer $l_{\rm ioni} \simeq 5$ mm contributes another $\tau_{\rm ioni} = l_{\rm ionie}/u$ to the total TOF-resolution $\tau_{\rm tot} = \sqrt{\tau_{\rm gate}^2 + \tau_{\rm ch}^2 + \tau_{\rm ioni}^2}$, such that the total relative TOF-resolution $\tau_{\rm tot}/\tau_{\rm max}$, where $\tau_{\rm max}$ denotes the most probable flight-time, is about 1.5% for CH_3F ($\tau_{\rm max} = 1.75$ ms, $u = 754$ m/s).

Table 3. Time-interval settings used in the TOF-measurements and the corresponding TOF-resolutions ("rps" stands for "revolutions per second"). See text for the definitions of the time intervals.

	CH_3F	He^*	Ne^*
Apparatus	A	B	B
Chopping method	random-sequence	single-slit	single-slit
Chopper-disk rot. speed	218 rps	350 rps	150 rps
τ_{gate}	18 μs	25 μs	60 μs
τ_{ch}	18 μs	7 μs	12.5 μs
τ_{ioni}	$\simeq 7\,\mu$s	–	–
τ_{tot}	26 μs	26 μs	61 μs
τ_{max}	1.75 ms	0.83 ms	2.0 ms
Resolution τ_{tot}/τ_{max}	1.5%	3%	3%

In Apparatus B a 142-mm-diameter chopper-disk with two diametrically opposite single-slits of identical truncated-wedge shape was spun at 350 (He^*) and 150 (Ne^*) revolutions per second. The slit width w decreased linearly with radius from $w_1 = 5$ mm at $R_1 = 53$ mm to $w_2 = 1$ mm at $R_2 = 68$ mm allowing to vary the gate-time by translating the chopper-disk, thereby varying the effective slit width $\tilde{w}$ at radius $\tilde{R}$ of the intersection of molecular-beam axis and chopper-disk resulting in a gate time $\tau_{gate} = \tilde{w}/(\tilde{R}\,2\pi\nu_{disk})$. Given the coarse positioning control of the chopper translation stage, $\tilde{R}$ and $\tilde{w}$ and, hence, τ_{gate} are known only approximately to be about $\tau_{gate} \simeq 25$ μs and $\tau_{gate} \simeq 60\,\mu$s in the He^* and Ne^* measurements, respectively. The signal was cyclically accumulated in 200 (He^*) and 265 (Ne^*) memory channels with a single-channel width of $\tau_{ch} = 7.0$ μs (He^*) and 12.5 μs (Ne^*). The total resolution of the TOF-measurement follows from convoluting both contributions to be $\tau_{tot} = \sqrt{\tau_{gate}^2 + \tau_{ch}^2}$. The contribution resulting from the finite length of the metastable-atom detector is negligible. The relative resolution is then calculated to be $\tau_{tot}/\tau_{max} \simeq 3\%$ for both, He^* ($\tau_{max} = 0.83$ ms) and Ne^* ($\tau_{max} = 2.0$ ms). The timings used in the TOF-measurements are summarized and compared for both apparatus in Table 3.

The mass spectrometric detection of polyatomic molecules is complicated by the fragmentation of the molecules upon electron impact ionization. Figure 2 shows mass spectra of CH_3F (a) and CHF_3 (b) beams at source pressures of $P_0 = 2$ and 4 bar, respectively, with the ion signal plotted on a logarithmic scale as a function of the ion mass. The dashed line shows the background mass spectrum without the molecular beam. For CH_3F, the carbon ion C^+ and the molecular ions CH^+, CH_2^+, CH_3^+, CF^+, CHF^+, CH_2F^+, and CH_3F^+ are all clearly observed as indicated in Figure 2. Rather weak signals on masses 19 and 20 amu are attributed to F^+ and HF^+ ions. Since the CH_3F^+ ion fragment at 34 amu has the most intense signal and a relatively low background count rate of only

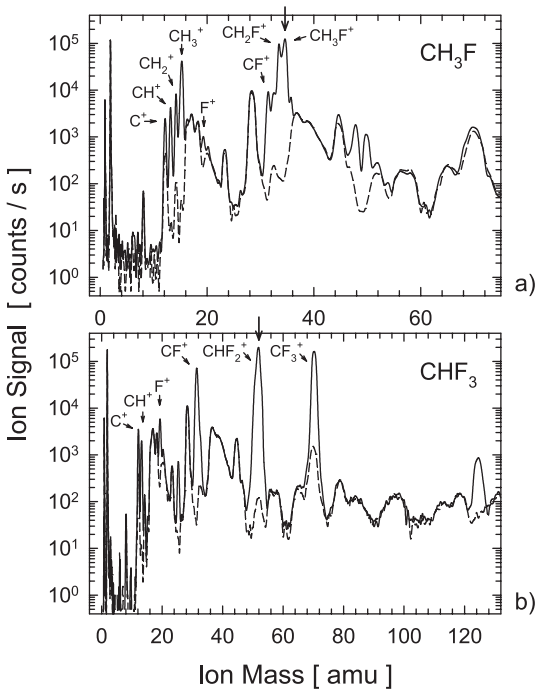

Fig. 2. Electron impact mass spectra of a CH_3F beam at $P_0 = 2$ bar (a) and of a CHF_3 beam at $P_0 = 4$ bar (b). The dashed lines represent the detector background signal. The arrows mark the peaks at ion masses of 34 amu and 50−51 amu at which the mass spectrometer was operated in the CH_3F and CHF_3 diffraction experiments, respectively.

100 counts/s, the mass spectrometer was operated at this mass in the diffraction experiments. The small intensities at larger masses, e.g. at 35 amu (CH_3FH^+), 47 amu (CH_3FCH^+), and 49 amu ($CH_3FCH_3^+$), which cannot result from ionization of monomers, confirm the presence of only a small amount of clusters in the beam.

For CHF_3 the situation is similar. Intense peaks are observed at masses of 31, 50, 51, and 70 amu corresponding to the fluoride fragment ions CF^+, CF_2^+, CHF_2^+, and CHF_3^+, respectively. The fragment peak at 50−51 amu has the highest intensity and a small background of only 100 counts/s and was therefore used for detecting CHF_3. As for CH_3F an appreciable amount of clusters could be ruled out by the weak signals at masses larger than 120 amu.

3 Results

3.1 Diffraction of CH_3F and CHF_3 beams

Total-intensity diffraction patterns for CH_3F are shown in Figure 3a for normal ($\Theta = 0$) and in Figure 3c for off-normal ($\Theta = 21°$) incidence. At normal incidence only the first order diffraction peaks are clearly resolved at diffraction angles of $\vartheta^{(1)} = \pm 200\,\mu$rad with peak heights of 800 counts/s. These peaks are significantly broader than the zeroth order central peak indicating the expected increase in peak width due to the relatively broad velocity

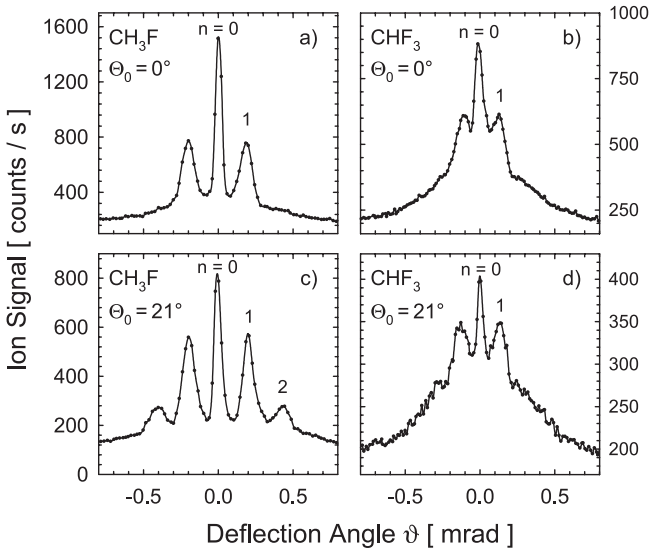

Fig. 3. Measured diffraction patterns of CH_3F and CHF_3 at normal ($\Theta_0 = 0°$; graphs (a) and (b), respectively) and off-normal ($\Theta_0 = 21°$; (c) and (d), respectively) incidence of the beam with respect to the plane of the diffraction grating. The source pressures are $P_0 = 1$ bar, 1.5 bar, 3 bar, and 1.5 bar in the measurements of (a), (b), (c), and (d), respectively. The numbers indicate the diffraction order n.

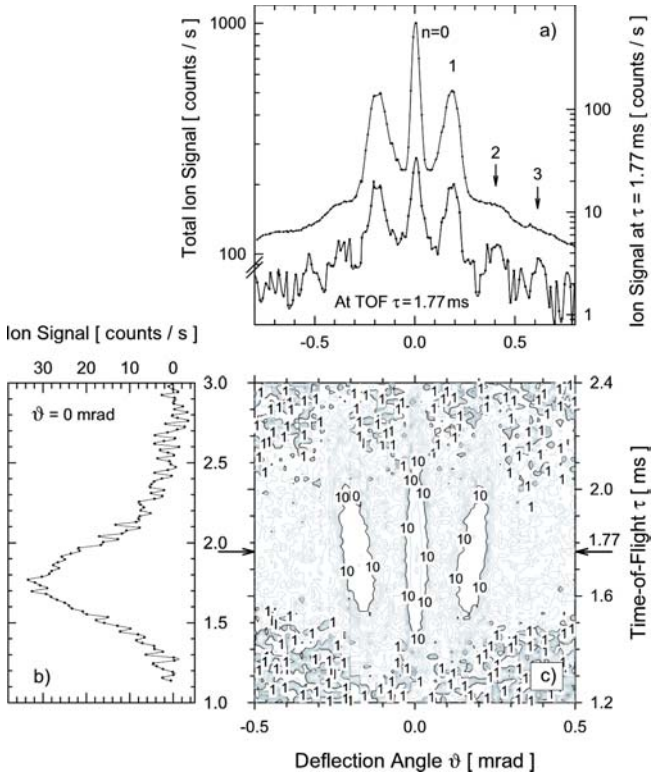

Fig. 4. Contour plot of flight-time resolved diffraction data of a CH_3F beam measured at normal incidence ($\Theta_0 = 0°$) and $P_0 = 2$ bar (c). A cross-section of the contour plot at a given deflection angle of $\vartheta = 0$ mrad is shown in (b). A cross-section of the contour plot at a time-of-flight of $\tau = 1.77$ ms (lower curve in (a)) is compared with the total-intensity diffraction pattern (upper curve in (a)).

distribution (Eq. (1)). In the off-normal position the effective grating period, i.e. the projection of the grating period in the beam direction [12], is reduced by about 7% and, hence, the resolution is increased revealing second order diffraction peaks at $\vartheta^{(2)} \approx \pm 400\,\mu$rad in addition to the first and zeroth order peaks. The factor two reduced intensity of the zeroth order peak is explained by the reduced transmission at off-normal incidence resulting from the finite thickness (depth) of the grating bars [12].

The analogous diffraction patterns for CHF_3 beams are shown in Figure 3b for normal and in Figure 3d for 21° incidence. As the de Broglie wavelength of the heavier CHF_3 is only $\lambda = 0.11$ Å (see Tab. 1), the diffraction angles are smaller than for CH_3F. For $\Theta_0 = 0°$ the first order diffraction peaks are resolved at $\vartheta^{(1)} = \pm 120\ \mu$rad with a peak height of 600 counts/s. As for CH_3F the first order peaks are slightly more distinct for $\Theta_0 = 21°$ because of the 7% increase in the diffraction angle and because of the increased ratio of first to zeroth order peak intensities resulting from the broadening of the slit function. Second or higher order diffraction peaks are, however, not resolved, but a wide pedestal is observed, the intensity of which decreases slowly from $|\vartheta| = 200$ to $600\,\mu$rad. This is attributed to the broader velocity distribution, which causes a spreading and overlapping of the second and third order peaks, as confirmed by the greater widths of the first order peaks compared to CH_3F.

The improvement provided by TOF-measurements is illustrated for CH_3F in Figure 4. At $P_0 = 2$ bar 120 TOF-distributions were measured at equidistant angular positions between $\vartheta = -0.8$ and 0.8 mrad. Each TOF-spectrum was integrated over 5 min resulting in an overall measuring time of more than 10 hours. A typical broad TOF-distribution measured for the zeroth order peak at $\vartheta = 0°$ is shown in Figure 4b. The maximum at $\tau_{\max} = 1.75$ ms corresponds to a (most probable) velocity of the CH_3F-molecules of $u = 754$ m/s, and its width (FWHM) of $\Delta\tau = 0.54$ ms indicates a beam velocity spread of $\Delta v/u = 31\,\%$. The range of flight-times extending from $\tau = 1.1$ to 3.0 ms corresponds to a range of velocities from 1200 to 440 m/s. In Figure 4c the TOF-spectra in the angular range from −0.5 to 0.5 mrad and for flight-times ranging from 1.2 to 2.4 ms are shown as a contour plot. The zeroth order peak is visible at flight-times between 1.45 and 2.1 m/s corresponding to velocities between 880 and 630 m/s, respectively. In addition, the first order peaks are clearly visible at diffraction angles increasing from 150 μrad at a flight-time of 1.5 ms to about 200 μrad at 2.1 ms.

The observed linear increase of the diffraction angles $\vartheta^{(n)}$ with flight-time τ is expected from the simple wave-optical condition for small diffraction angles [19],

$$\vartheta^{(n)} \approx \sin\vartheta^{(n)} = n\frac{\lambda}{d} = n\tau\frac{h}{dmL}\,, \qquad (2)$$

where m and h stand for the mass of the molecule and Planck's constant, respectively. In the limit of vanishing flight-times $\vartheta^{(n)} \to 0$ holds, which corresponds to the limit

of classical particle propagation. From the slope of the diffraction angle as a function of flight-time the product dm and hence, since d is known, the mass of the particle can, in principle, be determined.

The top curve in Figure 4a shows the total-intensity diffraction pattern, which is essentially similar to Figure 3a, but is characterized by an improved signal-to-noise ratio and is plotted on a logarithmic intensity scale. The first order peaks are clearly visible. Due to the velocity spread their FWHM $\Delta\vartheta^{(1)}$ of about 90 μrad is more than 2 times larger than the FWHM of the zeroth order $\Delta\vartheta^{(0)} = 40\,\mu$rad. Also the second order peaks are visible as shoulders at about ± 0.4 mrad. The third order diffraction peaks cannot be unambiguously identified at their expected positions indicated by an arrow in Figure 4a. Since, according to equation (1), the absolute broadening of the diffraction peaks due to the velocity spread increases with increasing diffraction order, the second order peaks are broader than the first order peaks and are no longer resolved.

The lower angular distribution in Figure 4a shows a cross-section of the contour plot at constant flight-time $\tau = 1.77$ ms. In this time-slice diffraction pattern the peak resolution is improved and, in addition to the zeroth and first order peaks, the second and even the third order peaks are fully resolved despite the factor 30 reduced peak intensities which are just above the noise level. The residual velocity spread is given by the TOF-resolution mentioned above to be $\Delta v/u = \tau_{\rm tot}/\tau_{\rm max} = 1.5\%$. By applying equation (1) it is expected to result in a negligible broadening of the diffraction peaks allowing to achieve high resolution that is limited by the beam collimation, i.e. by $\Delta\vartheta^{(0)}$ [2].

In Figure 5a the observed CH_3F total-intensity diffraction pattern from Figure 4a is re-plotted (points connected by a dashed line) and compared with a full simulation [12] (continuous line), in which a mean de Broglie wavelength λ_0 of 15.5 pm and a velocity spread $\Delta v/u$ of 44% were employed and a constant of 114 counts/s was added to account for the detector background signal. The best fit to the observed total-intensity diffraction pattern is achieved for the parameters $s_{\rm eff} = 34.5$ nm, $\delta = 7.0$ nm, $\sigma = 4.3$ nm, which describe the real and imaginary part of the effective slit width and random slit-width variations across the grating, respectively [7]. Both, the resulting difference between geometrical and effective slit width, $s_0 - s_{\rm eff} \simeq 19$ nm, and the δ-parameter are large compared to the corresponding values observed previously for rare gas atoms and diatomic molecules [7] and indicate a relatively strong interaction between the CH_3F-molecules and the surfaces of the grating bars. The calculation was repeated for a small velocity spread of $\frac{\Delta v}{u}$ =1% and a constant effective background of 0.8 counts/s, while keeping the other parameters identical. In Figure 5b this calculation is compared with the observed time-slice diffraction pattern at $\tau = 1.77$ ms flight-time copied from Figure 4a.

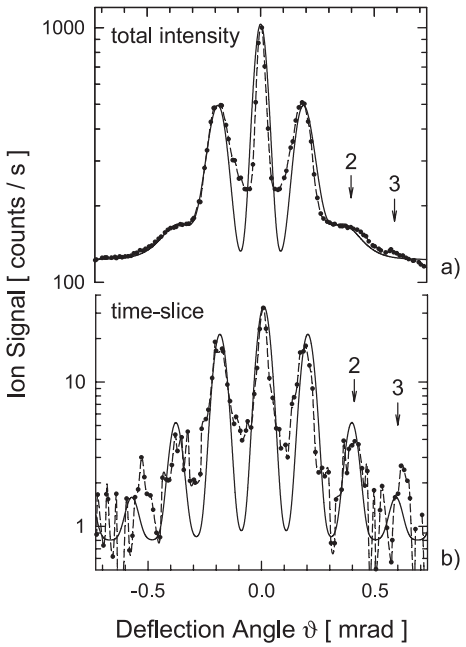

Fig. 5. Comparison of the measured total-intensity (a) and time-slice (b) diffraction patterns of a CH_3F beam (points connected by dashed lines, re-plotted from Fig. 4a) with full simulations (continuous lines) assuming an angular width $\Delta\vartheta^{(0)}$ of 50 μrad and a velocity spread $\Delta v/u$ of 44% and 1%, respectively.

The comparison of the observed total-intensity and time-slice diffraction patterns with the corresponding calculations in Figure 5 indicates, to a large extent, quantitative agreement between the data and the model calculation confirming that the increasing broadening results from the finite velocity distribution. The calculation in Figure 5b confirms the assignment of the weak peaks to second and third diffraction orders as indicated by arrows. Further, it confirms that, due to the narrow effective velocity distribution in the time-slice, full resolution of the diffraction peaks is restored as described above.

Appreciable deviations of the calculation from the observed data in Figure 5a occur only at the inner sides of the first order peaks and at the slight overestimation of the zeroth order peak width. These deviations are attributed to molecular clusters and small Fresnel corrections. In Figure 5b the deviations in peak widths and heights between experiment and calculation can be attributed mainly to noise in the observed data, while the relatively intense minima between zeroth and first order peaks, which have a much smaller minimum intensity in the calculation, are attributed to molecular clusters and small Fresnel corrections just as the deviations in Figure 5a. The discrepancies in the third-order peak positions are also partly attributed

[2] The widths of the first order peaks observed in the lower angular distribution in Figure 4a are about $\Delta\vartheta^{(1)} = 69\,\mu$rad, which is smaller than the corresponding value of 90 μrad in the total-intensity measurements but still significantly larger than the width of the zeroth order $\Delta\vartheta^{(0)} = 40\,\mu$rad. This residual broadening of the first order peak can be attributed to the low signal-to-noise ratio in the TOF-measurements which can be seen in Figure 4b for the most intense zeroth order and which is even stronger for the less intense first orders.

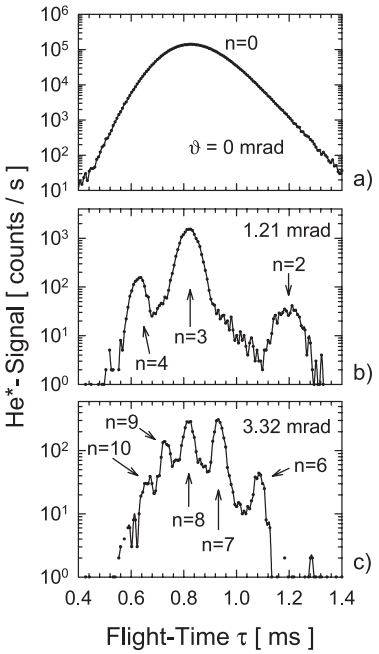

Fig. 6. Time-of-flight distributions of a metastable helium beam at $P_0 = 2\,\text{bar}$ and normal incidence on the grating. The detector was positioned at $\vartheta = 0$ (a), 1.21 (b), and 3.32 mrad (c). Each TOF-peak corresponds to a diffraction order n as indicated.

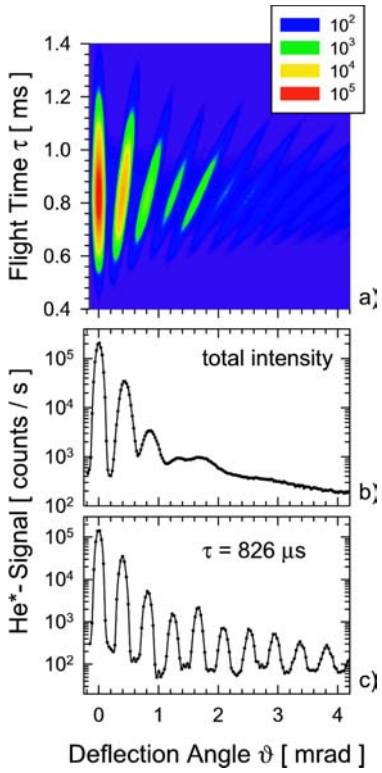

Fig. 7. Flight-time resolved diffraction data (a) and total-intensity diffraction pattern (b) of the metastable helium beam. In (c) a horizontal cut through the contour plot (time-slice) at a given flight-time of $\tau = 826\,\mu\text{s}$ reveals resolved diffraction peaks up to the ninth order which are obscured in the total-intensity diffraction pattern. The TOF-spectra shown in Figure 6 represent vertical cuts through the contour plot.

to a systematic error in the measurement of the small deflection angles, which has resulted in a small bogus angular asymmetry in measured diffraction patterns [12].

3.2 Diffraction of He* and Ne* beams

With the metastable atom beams, due to the larger overall signal, even more diffraction orders not resolved in the total-intensity diffraction pattern become visible by the time-of-flight technique. With a He* beam at $P_0 = 2\,\text{bar}$ and normal incidence on the grating 137 TOF-spectra were measured, for 5 min each, at equidistant detector positions between $\vartheta = -0.1$ and 4.25 mrad. In Figure 6 three of these TOF-distributions are shown. In the forward direction at $\vartheta = 0\,\text{mrad}$ one intense, broad peak is found and attributed to the zeroth diffraction order (Fig. 6a). In Figure 6b, for $\vartheta = 1.21\,\text{mrad}$, three narrower, fully resolved peaks appear at about $\tau = 0.6$, 0.8, and 1.2 ms. In Figure 6c, finally, for $\vartheta = 3.32\,\text{mrad}$, five even narrower peaks at about $\tau = 0.65$, 0.73, 0.82, 0.93 and 1.1 ms are resolved. Given the mass of the helium atom m_{He} and the flight-path length ($L = 1.95\,\text{m}$ for Apparatus B) the diffraction order n for each peak can easily be calculated from the time-of-flight using equation (2) and is indicated in the figure. The ratio of the orders n of any two peaks is just inverse to the ratio of the flight-times τ at the peak centers, as can easily be verified in Figure 6.

The decrease in width of the TOF-peaks with increasing n can be understood by the contour plot of the TOF-data in Figure 7a, where diffraction peaks up to the ninth order are clearly visible. With increasing diffraction order n the peaks are increasingly rotated in the τ-ϑ-plane around the origin. Thus, the peak width in a cut parallel to the flight-time axis for a given ϑ decreases with n^{-1}, reflecting the derivative $d\tau/d\vartheta = dmL/nh$ of equation (2). In addition, the contour plot illustrates how the smearing-out of the peaks in the total-intensity diffraction pattern plotted in Figure 7b results from the increasing overlap of peaks with increasing deflection angle. While at an angle of $\vartheta = 0.65\,\text{mrad}$ only the first and second order peaks overlap, at, e.g., $\vartheta = 2.77\,\text{mrad}$ the center part of the seventh order peak overlaps with the slow-atom part of the sixth and the fast-atom part of the eighth order peak and, as can be seen in the corresponding TOF-distribution, even with the very slow-atom tail of the fifth and the very fast-atom tail of the ninth order peak.

In the observed He* total-intensity diffraction pattern shown in Figure 7b only the zeroth, first, and second order diffraction peaks are well resolved while the third order peak at $\vartheta^{(3)} \simeq 1.3\,\text{mrad}$ is barely resolved from the fourth order peak, and higher order peaks are not resolved despite the relatively large signal of more than 200 counts/s up to $\vartheta = 4\,\text{mrad}$.

Figure 7c shows a time-slice of the contour plot at $\tau = 0.83\,\text{ms}$ corresponding to a velocity of 2347 m/s.

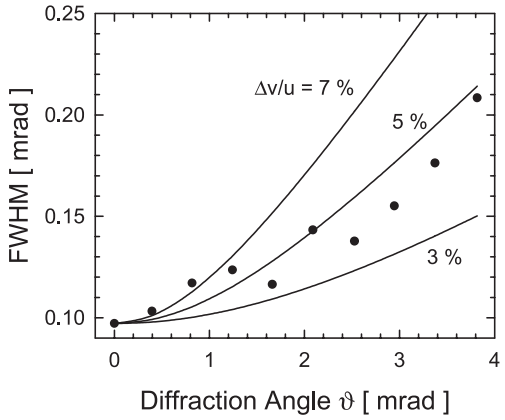

Fig. 8. Peak widths (FWHM) of the He* time-slice diffraction pattern shown in Figure 7c (points). From the comparison with calculations based on equation (1) assuming $\Delta v/u = 3$, 5, and 7% (lines) the effective velocity spread of the time-slice is found to be slightly larger than the calculated TOF-resolution listed in Table 3.

In the time-slice diffraction pattern all diffraction peaks within the angular range of the measurement are fully resolved, thereby demonstrating a striking improvement of resolution compared to the total-intensity data of Figure 7b. Quantitative analysis reveals that the angular width of the peaks in the time-slice increases only slightly from 0.1 mrad (FWHM) for the zeroth order to about 0.18 mrad for the eighth order peak as shown in Figure 8 (points). From a comparison with calculations based on equation (1) (lines) the effective relative velocity spread of the time-slice diffraction pattern is determined to be $3\% \leq (\Delta v/u)^{\text{eff}} \leq 5\%$ which is somewhat larger than the theoretical effective velocity resolution of the TOF-measurement of 3% as listed in Table 3. The slight discrepancy can be attributed to the uncertainty in the actual chopper-slit width $\tilde{w}$. It follows from equation (1) that for a velocity spread of only 3%, an angular width of the collimated molecular beam of $\vartheta^{(0)} \simeq 100\,\mu$rad, and the given diffraction angles of He* the diffraction peaks up to the 32th order will have a broadening smaller than the angular distance to the neighboring peaks and thus can, in principle, be resolved.

Similar experiments have been carried out for a metastable-neon atom-beam. Figure 9a shows data from 76 TOF-spectra measured at equidistant angles between $\vartheta = 0$ and 2.5 mrad. Diffraction peaks up to the ninth order are well resolved and easily identified. In the total-intensity measurement shown in Figure 9b the resolution is worse than for He*, which can easily be understood in terms of the smaller de Broglie wavelength and the broader velocity distribution (see Tab. 1); only the zero and first order diffraction peaks are resolved, while all the higher order peaks are completely smeared out.

At flight times of between about 3.3 and 3.4 ms and at angles smaller than about 0.7 mrad a stripe of increased intensity can clearly be seen in the contour plot in Figure 9a. It is attributed to UV-photons from the discharge source which can reach the detector and contribute to the

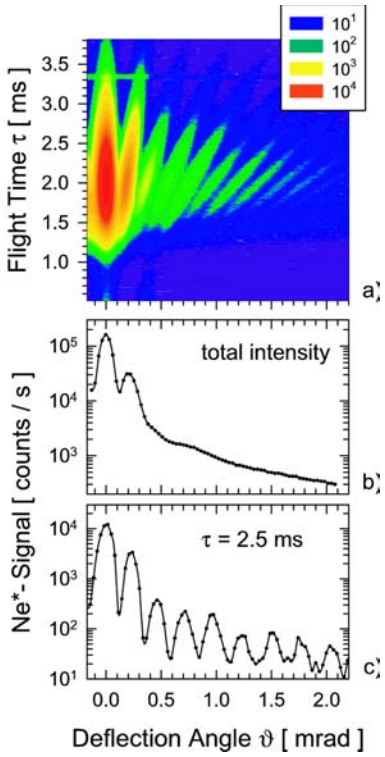

Fig. 9. Flight-time resolved diffraction data (a) and total-intensity diffraction pattern (b) of a metastable neon beam at $P_0 = 1.6$ bar and normal incidence on the grating. In (c) a horizontal cut through the contour plot (time-slice) at a given flight-time of $\tau = 2.5$ ms reveals resolved diffraction peaks up to the eighth order which are not resolved in the total-intensity diffraction pattern.

counting rate during the time the chopper slit crosses the beam axis (gate time). As their velocity is the speed of light, the UV-photons must have passed the chopper slit one chopping-cycle period later than the atoms. As the chopper speed is 150 revolutions per second and there are 2 cycles per revolution, the photon's delay is calculated to be $3\frac{1}{3}$ ms in agreement with the observation.

In Figure 9c a time-slice diffraction pattern for $\tau = 2.5$ ms is shown, determined from the data shown in Figure 9a. All peaks appear completely resolved with their widths increasing only slightly from 100 μrad (FWHM) for the zeroth-order peak to about 140 μrad for the eighth order. With an effective velocity spread in the time-slice of 3% (see Tab. 3) Ne*-diffraction peaks up to the $n = 30$th order can, in principle, be resolved with the given setup, whereas only the zeroth and first diffraction-order peaks are resolved in the total-intensity diffraction measurement shown in Figure 9b.

4 Conclusions

The time-resolved diffraction data shown in Figures 4, 7, and 9 represent a direct demonstration of the inverse proportionality between velocity and de Broglie wavelength

of a particle. In addition, it indicates that, by combining time-of-flight measurements with angular scans it is possible to observe highly-resolved diffraction patterns independent of the velocity distribution of the molecular beam. The achievable resolution is characterized by the zeroth-order peak width plus a small broadening of the higher-order peaks due to the residual width of the effective velocity distribution resulting from finite TOF-resolution. The zeroth-order peak width is limited by either the spatial coherence of the apparatus, i.e. the beam collimation, or by the lateral extension of the diffraction grating. To gain high resolution diffraction patterns from TOF-resolved diffraction data the intensity observed at a given flight-time is extracted to get a time-slice diffraction pattern. In the resulting intensity pattern as a function of deflection angle the broadening even of higher-order diffraction peaks can be negligibly small, depending on the time-of-flight resolution.

Thus, even for molecular beams with a velocity distribution too broad to allow for resolution of diffraction peaks in total-intensity measurements, the demonstrated method allows to observe high-resolution diffraction patterns. Thus, transmission grating diffraction can be resolved with this technique for beams which cannot be formed with a narrow velocity distribution.

The technique is excellently suited for intense beams with a broad velocity distribution because a large signal allows to observe the resolved peaks even for relatively high diffraction orders as shown above for metastable helium and neon beams. As the random-chopping technique reduces the overall intensity only by factor two, this method is also well suited for low intensity experiments as, e.g., in the diffraction of a thermal C_{60} or C_{70} beam [8]. Since, in addition, with the random-chopping technique the reduction of the signal-to-noise ratio caused by the loss of intensity is largely counteracted [20], this technique is especially advantageous for measurements suffering from a notoriously large detector background signal.

In the present application of this technique the time-of-flight resolved diffraction data has been used to estimate the long-range attractive van der Waals potentials $-C_3/z^3$ between the surface of the grating bars and the atoms or molecules. For CH_3F the C_3 constant has been found to be greater than expected, based on previous experiments for the rare gases [7]. Additional measurements are needed to establish the origin of the increased interaction with the grating bars. For metastable helium and neon atoms the C_3 constants have been found to be more than an order of magnitude larger than those of the corresponding ground state atoms in agreement with calculations based on Lifshitz's theory for the C_3 coefficient [11].

We wish to thank Tim Savas and Henry I. Smith, MIT, for providing the nanoscale transmission grating to us, and P. Fouquet and J. Pick for assistance with the metastable atom beam source. Further, we thank L.W. Bruch, R. Brühl, G.C. Hegerfeldt, T. Köhler, M. Lewerenz, J.R. Manson, M. Stoll, and C. Walter for many inspiring discussions.

References

1. D.W. Keith, M.L. Schattenburg, H.I. Smith, D.E. Pritchard, Phys. Rev. Lett. **61**, 1580 (1988)
2. O. Carnal, A. Faulstich, J. Mlynek, Appl. Phys. B **53**, 88 (1991)
3. W. Schöllkopf, J.P. Toennies, Science **266**, 1345 (1994)
4. M.S. Chapman, C.R. Ekstrom, T.D. Hammond, R.A. Rubenstein, J. Schmiedmayer, S. Wehinger, D.E. Pritchard, Phys. Rev. Lett. **74**, 4783 (1995)
5. W. Schöllkopf, J.P. Toennies, J. Chem. Phys. **104**, 1155 (1996)
6. W. Schöllkopf, *Beugung von Atom-, Molekular- und Clusterstrahlen an nanostrukturierten Transmissionsgittern*, Dissertation (Max-Planck-Institut für Strömungsforschung, Report 7/1999, ISSN 0436-1199, Göttingen, 1998)
7. R.E. Grisenti, W. Schöllkopf, J.P. Toennies, G.C. Hegerfeldt, T. Köhler, Phys. Rev. Lett. **83**, 1755 (1999)
8. M. Arndt, O. Nairz, J. Vos-Andreae, C. Keller, G. van der Zouw, A. Zeilinger, Nature **401**, 680 (1999)
9. R.E. Grisenti, W. Schöllkopf, J.P. Toennies, G.C. Hegerfeldt, T. Köhler, M. Stoll, Phys. Rev. Lett. **85**, 2284 (2000)
10. L.W. Bruch, W. Schöllkopf, J.P. Toennies, J. Chem. Phys. **117**, 1544 (2002)
11. R. Brühl, P. Fouquet, R.E. Grisenti, J.P. Toennies, G.C. Hegerfeldt, T. Köhler, M. Stoll, Ch. Walter, Europhys. Lett. **59**, 357 (2002)
12. R.E. Grisenti, W. Schöllkopf, J.P. Toennies, J.R. Manson, T.A. Savas, H.I. Smith, Phys. Rev. A **61**, 033608 (2000)
13. K. Hornberger, S. Uttenthaler, B. Brezger, L. Hackermüller, M. Arndt, A. Zeilinger, Phys. Rev. Lett. **90**, 160401 (2003)
14. O. Nairz, M. Arndt, A. Zeilinger, Am. J. Phys. **71**, 319 (2003)
15. Ch. Kurtsiefer, T. Pfau, C.R. Ekstrom, J. Mlynek, Appl. Phys. B **60**, 229 (1995)
16. Ch. Kurtsiefer, T. Pfau, J. Mlynek, Nature **386**, 150 (1997)
17. S. Nowak, Ch. Kurtsiefer, T. Pfau, C. David, Opt. Lett. **22**, 1430 (1997)
18. T.A. Savas, S.N. Shah, M.L. Schattenburg, J.M. Carter, H.I. Smith, J. Vac. Sci. Technol. B **13**, 2732 (1995)
19. M. Born, *Optik*, 3rd edn. (Springer, Berlin, 1972)
20. D.J. Auerbach, in *Atomic and Molecular Beam Methods* edited by G. Scoles (Oxford University Press, Oxford, 1988), Vol. I, Chap. 14